

High-sensitivity and high-resolution collaborative determination of birefringence coefficient using weak measurement

Yanqiang Guo^{1,2,3}, Jiahui Hou^{1,2,3}, Min Zhang^{1,2}, Ao Wang^{1,2}, Shuqi Gao^{1,2},
Qingchen Liu^{1,2}, Hongyu Li^{2,3}, Xiaomin Guo^{1,2,3,*} and Liantuan Xiao^{1,2,3,*}

¹Key Laboratory of Advanced Transducers and Intelligent Control System, Ministry of Education,
College of Physics, Taiyuan University of Technology, Taiyuan 030024, China

²College of Physics and Optoelectronics, Taiyuan University of Technology, Taiyuan 030024, China and

³Shanxi Key Laboratory of Precision Measurement Physics,
Taiyuan University of Technology, Taiyuan 030024, China

(Dated: April 23, 2025)

We present a high-sensitivity and high-resolution birefringence coefficient determination system for nm-level membrane films based on weak measurement, addressing the sensitivity-resolution trade-off. A tunable bandwidth light source is exploited to achieve complementary momentum (P-pointer) and intensity (I-pointer) measurements, enabling calibration-free operation across various bandwidths, and to realize high-precision phase difference monitoring of the measured membranes. This method maps the birefringence effect to a weak-value amplified signal of spectral shift and light intensity. The optimal resolution, achieved at a spectral width of 6 nm, is 1.5×10^{-8} RIU, while the optimal sensitivity is achieved when the light source is a narrow-linewidth coherent laser, reaching 4710 mV/RIU. The linear range of the system covers a broad birefringence coefficient range for crystals, from 10^{-6} to 0.1. Furthermore, the auxiliary optical path eliminates substrate interference, achieving a detection limit of the birefringence coefficient as low as 10^{-8} RIU. This approach, characterized by high precision, high sensitivity, and strong robustness, provides an effective solution for the detection of optical nano-thin membrane parameters.

Birefringence coefficient is a key physical parameter of optical membranes[1–4] and directly influences the polarization characteristics[5, 6], transmission efficiency[7] and stability[7, 8] of the corresponding optical devices. And it is one of the most concerning indicators when it refers to the designing and optimizing of optical films[10, 11]. Moreover, the birefringence coefficient can be measured by polarization optical instruments and optical interferometers[12, 13]. The results obtained by the polarization optical instruments are extremely sensitive to the thickness and surface quality of the samples, which restricts its accuracy[14, 15]. Although the birefringence coefficient with high accuracy can be obtained through optical interferometers, the operational complexity and the rigorous test environment requirements limit its applications[16, 17]. Moreover, most of the existing measurement technologies generally face issues such as limited coherence of light sources and low measurement efficiency, making it difficult to meet the practical demands for high precision and effective detection[18, 19]. This is especially true in scenarios like micro/nano thin membrane property analysis or complex structure processing, where the limitations of traditional methods are further highlighted[20]. The rigorous requirements for sample surface morphology, environmental stability, or dynamic processes often lead to a decrease in the reliability of measurement results[21]. Therefore, there is an urgent need to develop more efficient and versatile measurements to overcome the existing barriers in precision and sensitivity.

In recent years, quantum weak measurement, with its high sensitivity and anti-noise capabilities, has provided a new

approaches for detecting small physical quantities, which can be applied to develop birefringence coefficient measurement technology[22–26]. The measurement uses the weak value amplification effect to transform the undetectable measurement-targeted parameters into observable light intensity or spectral shift signals to significantly improving measurement resolution[27–30]. Currently, weak measurement is constrained by the spectral width fluctuations of light sources and the noise of system, which restricts measurement accuracy and dynamic range[31–33]. For instance, narrow-spectral light sources lack sufficient sensitivity for light intensity indicators[34–37], while wide-spectral light sources are prone to momentum spectral broadening errors[38–42], thereby making it difficult to meet robustness requirements across various scenarios.

To address these challenges, this work presents a high-sensitivity and high-resolution nanometer-level birefringence coefficient detection system for thin membranes based on weak measurement. The complementary momentum P and intensity I dual-parameter measurements are designed. The measurements are also combined with shared optical paths that require no recalibration across different bandwidths, and phase difference detection to constitute the thin membrane birefringence coefficient measurement system. The system synchronously maps the birefringence effect into weak amplified signals of spectral shift and light intensity variation. We achieve optimized resolution for both the P-pointer and I-pointer across a range of spectral conditions, from narrow to wide bandwidths. The resolution of the P-pointer is on the order of 10^{-8} RIU, significantly higher than the 10^{-4} RIU resolution of ellipsometry. In addition to maintaining high resolution, the system eliminates substrate interference through an auxiliary optical path, achieving highly linear detection of the birefringence coefficient, with the I-pointer sensitivity reach-

*Electronic mail: guoxiaomin@tyut.edu.cn; xlt@sxu.edu.cn

ing above 4.7×10^3 mV/RIU exceeding current surface plasmon resonance detection methods. Its synergistic mechanism demonstrates the complementary advantages of variable bandwidth, with a wider spectrum optimizing the dynamic range and noise immunity of the P-pointer, and a narrower spectrum enhancing the sensitivity of the I-pointer. Furthermore, by introducing high-gain detection and dynamic noise suppression strategies, the system maintains a high and robust signal-to-noise ratio in complex noise environments. The measurement system exhibits the advantages of high resolution, high sensitivity, operational simplicity, and strong robustness, which provides an useful solution for the precise measurement of optical thin membrane parameters.

We first introduces an optimized shared optical path weak measurement system, which is used to measure small phase differences φ . The initial polarization of the system is $|\psi_i\rangle = (1/\sqrt{2})(|H\rangle+|V\rangle)$, and the momentum spectrum distribution of the light source is represented as $|\phi(p)\rangle$. The photon momentum is $p_0 = \omega_0/c$, where ω_0 represents the central frequency corresponding to the center wavelength λ_0 of the incident light, and c is the speed of light.

In weak interaction, one of the HWPs (Half-Wave Plates) is tilted by a small angle of θ to introduce an extremely small net phase shift of Δ between light o and light e . The phase shift is related to the birefringence effect. The mapping relationship between Δ and θ is:

$$\Delta = \pi \left(\frac{L}{L_0} - 1 \right) - \pi \left(\frac{1}{\sqrt{1 - \frac{\sin^2 \theta}{n^2}}} - 1 \right), \quad (1)$$

where L_0 is the actual thickness of the HWP, L is the length of the light wave passing through the tilted HWP, and $n = 1.54$ is the refractive index corresponding to the true zero-order HWP at 1550 nm in the experiment.

The first-order approximation model demonstrates nearly identical wavelength shifts across weak interactions, thereby enabling precise birefringence coefficient measurement. The quantitative correspondence between birefringence coefficient and phase shift is derived as:

$$\Delta\varphi = \frac{2\pi}{\lambda} \cdot \Delta n \cdot d \cdot \frac{1}{\cos \theta}. \quad (2)$$

Here, $\Delta = \Delta\varphi$, $\lambda = 1550\text{nm}$, and Δn represent the birefringence coefficients of the test sample that this paper focuses on, d is the film thickness, and $1/\cos \theta$ reflects the modulation effect of the tilt angle on the optical path difference. Additionally, an auxiliary optical path is established as a monitoring path to ensure $\theta = 0$.

The P-pointer was analyzed. The meter state is initialized to $\int dp |\phi(p)\rangle$, which is a Gaussian function with center p_0 and standard deviation σ_p . The interaction strength $g = \Delta n \cdot d$ can be derived from the weak interaction between the target quantum system and the meter state. For the weak interaction, the interaction operator is represented as $\hat{U} = \exp(ig/2\hat{A} \otimes \hat{P})$, where $\hat{A} = |H\rangle\langle H| - |V\rangle\langle V|$ is the observable of the target system, and \hat{P} is the momentum operator of

the meter state. Post-selection is subsequently performed on the system within the selected projection basis, typically projected onto a state that is nearly orthogonal to the initialization $|\psi_f\rangle = 1/\sqrt{2}(e^{i\rho}|H\rangle - e^{i\rho}|V\rangle)$, where ρ is the post-selection angle. Post-selection induces the collapse of the measurement instrument state into an unnormalized redistribution as $D(p) = \Phi(p)/2[1 - \cos(kp + 2\rho)]$, $\Phi(p) = |\langle\phi(p)|\phi(p)\rangle|^2$ is the spatial distribution of the initial momentum and p is the eigenvalue of \hat{P} . When $\rho \leq 1$, the post-selection causes the measurement instrument state to collapse into a bimodal distribution. The observable post-selection probability is $P_S \approx \sin^2(\rho)$, and the weak value $\langle\hat{A}\rangle_w$ can be obtained:

$$\langle\hat{A}\rangle_w = \frac{\langle\psi_f|\hat{A}|\psi_i\rangle}{\langle\psi_f|\psi_i\rangle} = i \cot(\rho). \quad (3)$$

It is noteworthy that the interaction strength g can be extracted from the offset of the average value of the P-pointer, and the expression is:

$$\begin{aligned} \Delta p &= \frac{\int p D(p) dp}{\int D(p) dp} - p_0 \\ &= \frac{1}{2P} \sigma_p^2 g e^{-\sigma_p^2 g^2} \sin(gp_0 + 2\rho) \\ &\approx g \sigma_p^2 \text{Im}(\langle\hat{A}\rangle_w), \end{aligned} \quad (4)$$

The weak measurement approximately satisfies $gp_0/2 \ll \rho \ll 1$.

After the weak interaction and the post-selection, the average horizontal displacement Δp of the photon momentum P-pointer in the collapsed measurement state, and the vertical displacement Δl of the total light intensity I-pointer can be observed. Wide incident spectra enhance ΔP dominance, whereas narrowed spectra intensify ΔI shifts; while when the incident spectrum narrows gradually, the displacement effect of the I-pointer becomes more pronounced. Specifically, when single-mode coherent light is incident, the weak interaction is entirely converted into a vertical light intensity displacement, resulting in negligible horizontal displacement of the meter state. Notably, high-precision measurement across varying spectral incident states cannot be achieved using a single pointer.

Given that the light intensity I-pointer represents intensity quantity, the initial light intensity without post-selection is denoted by I_{init} . After implementing weak interaction and post-selection $|\psi_f\rangle$, the light intensity received by the detector evolves to $I_S = I_{init} P_S$. The shift of I-pointer is:

$$\begin{aligned} \Delta l &= \frac{\Delta I_S}{I_S^{g=0}} = \frac{I_S - I_S^{g=0}}{I_S^{g=0}} \\ &\approx e^{-\sigma_p^2 g^2} p_0 g \text{Im}(\langle\hat{A}\rangle_w). \end{aligned} \quad (5)$$

The phase difference measurement accuracy δg is given by the following formula:

$$\delta g = \frac{\delta m}{\left(\frac{\partial S}{\partial g} \right)}, \quad (6)$$

where δm is the measurement resolution of the P-pointer (determined by the detection of the momentum spectrum distribution) or the intensity uncertainty of the I-pointer. S corresponds to $\Delta\rho$ and Δl , and $\partial S/\partial g$ represents the shift rate.

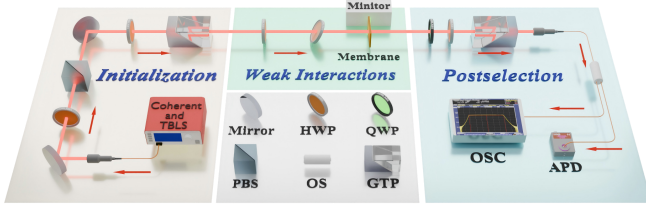


FIG. 1: Experimental schematic of high-sensitivity and high-resolution with weak measurement. TBLS: tunable bandwidth light source; HWP: half-wave plate; PBS: polarization beam splitter; PBD: polarization beam displacer; QWP: quarter-wave plate; GTP: Glan-Taylor polarizer. Film: The replacement positions of different thin membrane slide; Monitor: monitoring the angle of the tested slide. The final meter state through an optical switch (OS) either into the spectrometer for measuring the shift of the P-pointer or into the avalanche photodiode (APD) for measuring the shift of the I-pointer.

The principle of detecting the birefringence coefficient of thin membranes using the shared optical path weak measurement system is shown in Fig. 1. A tunable bandwidth light source (TBLS) with flat 1550nm-centered spectrum and a 400kHz narrow-linewidth coherent source are used. The system uses polarization degree of freedom of the photon as the system observables and momentum spectrum as the measurement instrument state. The pre-selection module combines a HWP and Glan-Taylor prism (GTP) to align partially polarized light's main axis with the GTP transmission axis. Weak coupling occurs through two near-orthogonal HWPs, where one is tilted to create a controlled phase delay. The test sample is placed after this stage, with an auxiliary path monitoring tilt consistency. Post-selection employs a quarter-wave plate (QWP), HWP and GTP combination to generate circular polarization components for imaginary weak value detection. To achieve a high signal-to-noise ratio, we employ the high-stability coherent laser source with a linewidth of 400 kHz and an high-gain avalanche photodiode (APD). Dynamic filtering and repeated measurements are used to suppress noise impacts. And the wide spectral characteristics of the TBLS ensures high signal-to-noise ratio and accuracy amidst noise.

In the P-pointer experiments, the spectral width is set to 0.5 nm, 1 nm, 3 nm, and 6 nm. The test sample is a 2 mm glass slide carries a 5 nm-thick membrane, denoted as $d = 5$ nm. Due to the glass substrate's dispersion affecting center wavelength position and light intensity, an uncoated glass slide serves as a control to eliminate substrate interference, enabling precise measurement of the film's birefringence coefficient. System calibration prioritizes dual-peak regions where weak measurement advantages maximize accuracy. The system's pre-selection angle is modified by replacing the thin membrane slides with different birefringence coefficients to explore the impact on the center wavelength and intensity shifts. After stabilization, spectral measurements are recorded using a 0.04 pm-resolution spectrometer.

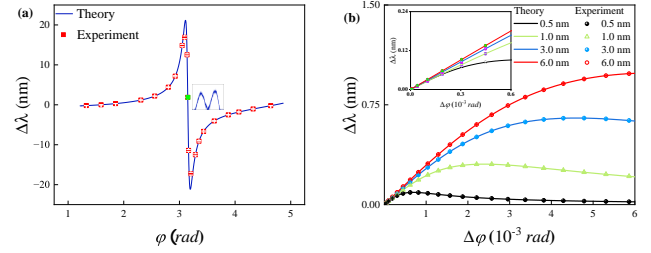


FIG. 2: (a) Results of spectral shift versus phase difference. The squares represent experimental data and the solid line represents the theoretical result. (b) Results of phase difference versus spectral shift for spectral widths.

Fig 2(a) shows the experimental and theoretical results of spectral shift as a function of the phase difference. The center wavelength shift exhibits a three-stage nonlinear response to rotation angle: initial gradual increase, rapid decay at peak angle, then slow recovery. This non-monotonic variation characteristic visually reveals the ultra-sensitive response mechanism of the weak measurement system to changes in the rotation angle, corresponding to the birefringence effect, where small phase differences induce significant center wavelength displacement. Optimal observation requires selecting linear-response regions while balancing sensitivity and measurement stability. Fig 2(b) further shows the correspondence between spectral shift and phase difference. At $\rho = 0.002$ rad and initial phase difference of $\gamma\rho \sim (19/10)\pi$, the optimal agreement between theory and experiment is achieved. From a spectral width of 0.5 nm to 6 nm, as the TBLS spectral width increases, for the same $\Delta\phi$, higher $\Delta\lambda$ corresponds to higher sensitivity, measurement accuracy and a larger linear range. When $\Delta\phi$ is in the range of $(0, 3 \times 10^{-3}$ rad), the spectral width of 6 nm has the largest linear range. According to Eq 2, the range of Δn at this point is $(0, 0.148)$, which aligns with the birefringence coefficient of typical crystals. Consequently, this study makes full use of this characteristic and identifies it as the optimal working region for high-sensitivity detection of various thin membranes. The squares represent the experimental results, while the solid lines correspond to the theoretical simulation results from Eq 4. Using Eq 6 and the TBLS with spectral widths of 0.5 nm, 1.0 nm, 3.0 nm, and 6.0 nm prepared experimentally, the measured linear phase difference shift rates of $\Delta\lambda/\Delta\phi$ are 285 nm/rad, 250 nm/rad, 163 nm/rad, and 44 nm/rad, respectively. The corresponding phase difference accuracies are 9.09×10^{-7} rad, 1.57×10^{-7} rad, 1.16×10^{-7} rad and 1.14×10^{-7} rad, respectively. On this basis, the 6 nm is selected as the optimal bandwidth for further investigation, with the experiment conducted at a temperature of 25 ± 0.5 °C. Notably, the system achieves a high resolution of 1.5×10^{-8} RIU and a high sensitivity of 2663 nm/RIU, demonstrating high performance in both sensitivity and resolution.

Initially, the spectrum displays a broad plateau around 1550 nm. Under weak measurement via post-selection, this transitions from a flat-top profile to a double-peak structure, as shown in Fig 3(a). Subsequent analysis focuses on center wavelength shifts induced by thin membranes with different

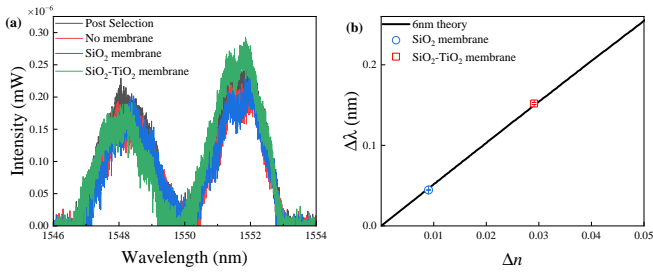


FIG. 3: (a) Measured spectra; (b) Linear fitting of spectral shifts for a spectral width of 6 nm, with error bars representing the standard deviation of 20 measurements.

birefringence coefficients. To balance linearity and accuracy, a 6 nm spectral width is selected for measurements. As shown in Fig 3(b), the birefringent coefficient change induced by a SiO_2 thin membrane slide is measured to be 0.009 RIU, while the birefringent coefficient change induced by a $\text{SiO}_2 - \text{TiO}_2$ thin membrane slide is measured to be 0.0291 RIU. Compared to the uncoated slide, these membranes induce center wavelength shifts of 0.0446 nm and 0.1520 nm, respectively. System stability is confirmed using 20 repeated measurements, with the standard deviation calculated from the averaged data being 4.12×10^{-8} nm.

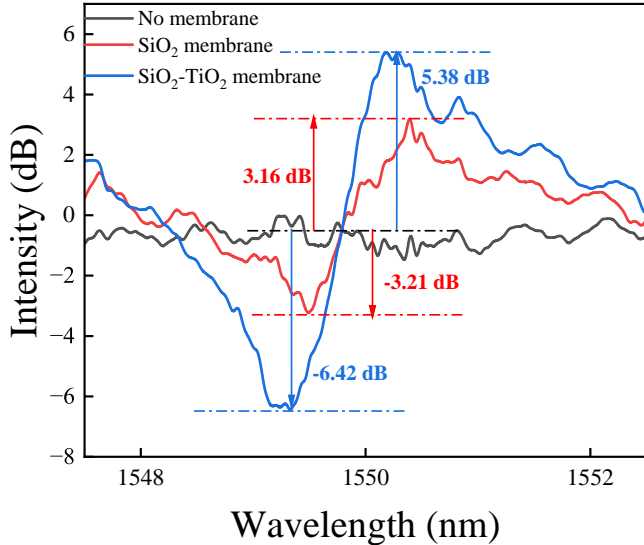


FIG. 4: Relative intensity results based on the dual-peak state serving as the reference under a 6 nm broadband light source.

Fig 4 shows relative intensity variations under different membranes. Using uncoated glass as a baseline, a SiO_2 membrane induces +3.16 dB and -3.21 dB intensity shifts, corresponding to approximately 50% signal change, attributed to birefringence differences between the membrane and air. A $\text{SiO}_2 - \text{TiO}_2$ membrane produces +5.38 dB and -6.21 dB shifts, exceeding fourfold intensity enhancement, with superimposed birefringence effects amplifying bimodal signals.

Introducing the I-pointer to validate the P-pointer reveals a 6nm TBLS double-peak distribution signal-to-noise ratio

(SNR) of 11.5 dB, while 0.5 nm TBLS shows 2.5 dB, representing the resolution limit under present experimental constraints. Reducing spectral width improves sensitivity, but single-mode lasers fail to resolve bimodal peaks due to electronic noise. APD-based post-selection achieves 17.5 dB SNR for single-mode lasers. The final data are collected using a 6 GHz real-time oscilloscope. Consequently, the P-pointer and I-pointer achieve complementarity in high resolution and high sensitivity.

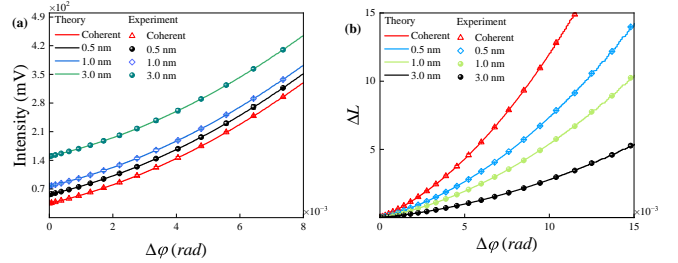


FIG. 5: (a) Total intensity of various spectral width light sources measured by the APD after passing through the thin membrane and post-selection; (b) I-pointer shift ΔL passing through the thin membrane as a function of phase difference $\Delta\phi$. The error bars represent the standard deviation of twenty repeated experiments.

Similarly, the weak measurement system is initially placed near the dual-peak working region, and then a phase difference is introduced by rotating the glass slide of the monitoring system to evaluate the overall system performance. Fig 5 illustrates the post-selection light intensity and shift ΔL of the I-pointer as a function of the $\Delta\phi$. In Fig 5(a), the intensity increases with the spectral width. This trend is attributed to the fact that the broader spectral width results in the higher SNR after post-selection. Fig 5(b) shows an inverse relationship between the intensity shift of the I-pointer and the incident spectral bandwidth, exhibiting a contrasting trend to that of the P-pointer. This experimental results agree well with the theory, where under narrow-spectrum illumination, the meter state demonstrates an evident longitudinal shift but minimal transverse shift, corresponding to a noticeable I-pointer shift and negligible P-pointer shift. According to Eq 6, the intensity departure for coherent light and TBLS with spectral widths of 0.5 nm, 1.0 nm, 3.0 nm are 0.044 mV, 0.072 mV, 0.11 mV, and 0.21 mV, respectively, and the corresponding phase difference accuracy δg is 2.02×10^{-6} rad, 3.17×10^{-6} rad, 4.83×10^{-6} rad and 9.37×10^{-6} rad. On this basis, the coherent laser is chosen as the optimal illumination for further investigation, notably achieving a high sensitivity of 4710 nm/RIU and a high resolution of 9.34×10^{-6} RIU. The sensitivity is above 1500 nm/RIU higher than that of existing surface plasmon resonance detection, and the resolution is sufficient to cover the range of birefringence coefficients for typical crystals.

For the intensity changes and I-pointer shifts caused by different birefringent coefficient thin membrane slides in the above experiment, further processing and analysis are carried out. As depicted in Fig 6(a), to optimize the balance between the largest linear region and the lowest SNR, we select a coherent laser with a linewidth of 400 kHz as the main measure-

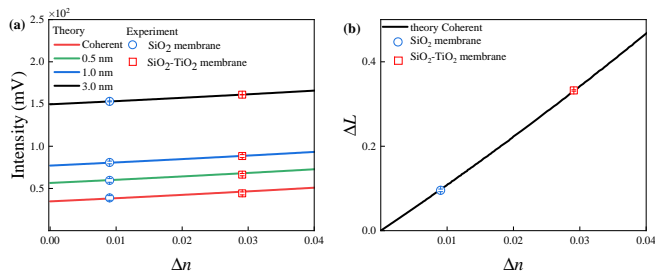


FIG. 6: (a) Linear correspondence between the intensity and the birefringence coefficient measured by APD under various spectral widths and after different films and post-selection; (b) linear correspondence between the birefringence coefficient and the I-pointer shift.

ment. In Fig 6(b), the birefringent coefficient change caused by a SiO₂ membrane and a SiO₂ – TiO₂ is 0.009 RIU and 0.0291RIU, respectively. This result is consistent with the P-pointer measurement data, further validating the feasibility of measurements using both the P and I pointers. Relative to the uncoated slide, the SiO₂ membrane causes an I-pointer shift of 0.0955, while the SiO₂ – TiO₂ membrane shifts it by 0.3322. System stability is validated through 20 repeated measurements, with standard deviations calculated from averaged I-pointer shifts. Post-stabilization, the birefringence coefficient’s standard deviation (1.12×10^{-6}) is derived from 20 I-pointer shift measurements.

The results indicate that the high sensitivity of the I-pointer enables it to respond effectively to minute signal changes, making it particularly suitable for continuous monitoring of weak signals under low SNR conditions. But its resolution is inferior to that of the P-pointer. In contrast, the P-pointer has lower sensitivity but achieves nanometer-level resolution,

providing higher stability and a smaller error range. The P-pointer can maintain stable resolution capabilities in complex noise environments.

In conclusion, this work introduces and experimentally validates a high-sensitivity and high-resolution weak measurement system for nanoscale membrane birefringence coefficient determination. By synergistically employing tunable-bandwidth light and coherent light sources, the complementary advantages of variable bandwidth are fully demonstrated. The tunable bandwidth light optimizes the dynamic range and noise immunity of the P-pointer, while the coherent light enhances the sensitivity of the I-pointer, all achieved calibration-free operation across various bandwidths. When the spectral width is 6 nm, the system achieves the best resolution of 1.5×10^{-8} RIU, significantly outperforming traditional ellipsometers. The optimal sensitivity is achieved with the narrow-linewidth coherent laser, reaching 4710 mV/RIU, which surpasses existing surface plasmon resonance measurements by above 1500 mV/RIU. The system’s linear range is from 0 to 0.148, fully covering the birefringence coefficient range of the typical crystals. Moreover, the setup of the auxiliary optical path eliminates substrate interference, thereby extending the detection limit to 10^{-8} RIU. Our work develops a high-precision and robust solution for optical quantum measurement of advanced nonmaterial in challenging environments.

The authors thank Professor Guohui Li for his valuable assistance during the membrane preparation stage. This work was supported by the National Key Research and Development Program of China (2022YFA1404201), the National Natural Science Foundation of China (62175176, 62475185, and U23A20380), and the Fundamental Research Program of Shanxi Province (Grant No. 202403021221034).

- [1] J. Wang, E. Wang, X. Cui, P. Li, Q. Jing, and Z. Chen, “The birefringence in orthorhombic and triclinic lead-iodates and the functional basic units’ contribution: A first-principles investigation,” *Chem. Phys. Lett.* **867**, 141987 (2025).
- [2] M. Seigo, H. Fukui, S. Kawano, and M. Kupinski, “Inhomogeneous birefringence analysis using a tensor-valued backprojection,” *Opt. Rev.* **59**, 278 (2025).
- [3] T. Wang, H. Luo, S. Zhang, L. Huang, L. Cao, X. Dong, and G. Zou, “Enhanced Birefringence and Excellent Thermal Stability in Two Tellurium(IV) Vanadates: KTeOVO₄ and Ca₂TeV₂O₉,” *Inorg. Chem.* **64**, 4673 (2025).
- [4] Z. Xue, X. Wen, Y. Yan, J. Chen, Z. Hu, J. Wang, N. Ye, and G. Peng, “Lithium Borate-Square: An Organic–Inorganic Groups-Mixed Nonlinear Optical Crystal with Large Birefringence,” *Inorg. Chem.* **64**, 3637 (2025).
- [5] E. E. Fouché, G. W. Bosman, and P. H. Neethling, “Polarization-sensitive Fourier ptychographic microscopy for high-resolution, large area birefringence imaging of petrographic thin sections,” *J. Phys.: Conf. Ser.* **2970**, 012007 (2025).
- [6] X. Theillier, S. Rivet, M. Dubreuil, and Y. Le Grand, “Swept-wavelength null polarimetry for highly sensitive birefringence laser scanning microscopy,” *Opt. Lett.* **49**, 387 (2024).
- [7] Y. Zhou, L.-T. Jiang, X.-M. Jiang, B.-W. Liu, and G.-C. Guo, “Mixed-anion square-pyramid [SbS₃I₂] units causing strong second-harmonic generation intensity and large birefringence,” *Chin. Chem. Lett.* **36**, 109740 (2025).
- [8] A. Brozyniak, K. Stadlmann, P. Kürnsteiner, and H. Groiss, “Optimized procedure for conventional TEM sample preparation using birefringence,” *Micron* **177**, 103580 (2024).
- [9] X. Guo, R. Liu, P. Li, C. Cheng, M. Wu, and Y. Guo, “Enhancing Extractable Quantum Entropy in Vacuum-Based Quantum Random Number Generator,” *Entropy* **20**, 819 (2018).
- [10] H. Kuratsuji, “Optical skyrmions in nonlinear birefringence media: semiclassical approach incorporating effective gauge field,” *J. Opt.* **27**, 015501 (2025).
- [11] D. O. Dorohoi and D. G. Dimitriu, “A Spectral Method for Rapidly Determining the Linear Birefringence of Thin Polymer Films,” *Molecules* **29**, 6007 (2024).
- [12] B. Baradaran, A. J. Black, S. R. Heilbronner, and T. Akkin, “Visible light polarization-sensitive optical coherence tomography with balanced detection,” *J. Biomed. Opt.* **30**, 036002 (2025).
- [13] D. Im, Z. M. F Aziz, F. Jin, J. S. Kim, E. Magee, P. Amarasinghe, S. Trivedi, and M. T. Zanni, “Achromatic correction for birefringent interferometers that improve Fourier transform spec-

- trometers and hyperspectral imaging,” *Opt. Express* **32**, 538565 (2024).
- [14] Z. Ma, N. Gu, J. Zhang, and A. Tang, “Achromatic correction for birefringent interferometers that improve Fourier transform spectrometers and hyperspectral imaging,” *Appl. Phys. B* **10**, 167 (2025).
- [15] S. Roussel, M. Boffety, and F. Goudail, “Polarimetric precision of micropolarizer grid-based camera in the presence of additive and Poisson shot noise,” *Opt. Express* **26**, 29968 (2018).
- [16] Y. Sun, W. Zhou, Z. Liu, W. Li, S. Jiang, L. Liu, Y. Jiang, and W. Wang, “Large-format grating groove density measurement method based on optical interferometry,” *Opt. Lasers Eng.* **187**, 108885 (2025).
- [17] Y. Zheng and C. Jiang, “Experimental Investigation of an Incremental Contact Model for Hyperelastic Solids Using an In Situ Optical Interferometric Technique,” *Lubricants* **12**, 109 (2024).
- [18] S. Kim, Y. Kim, N. Sugita, and M. Mitsuishi, “Surface measurement of silicon wafer using harmonic phase-iterative analysis and wavelength-scanning Fizeau interferometer,” *Precis. Eng.* **75**, 142 (2022).
- [19] F. J. Torcal-Milla, J. Lobera, A. M. Lopez, V. Palero, N. Andres, and M. P. Arroyo, “Mach-Zehnder-based measurement of light emitting diodes temporal coherence,” *Optik* **267**, 169722 (2022).
- [20] T. Wang, L. Wang, N. Ma, Y. Zhang, L. Liu, Y. Wan, L. Zhou, and W. Qian, “Nanoporous Polystyrene Inverse Opal Materials with Optical Interference Properties for Label-Free Biosensing,” *Langmuir* **40**, 19517 (2024).
- [21] X. Ling, S. Liu, and X. Liu, “Enhancement of laser-induced damage threshold of optical coatings by ion-beam etching in vacuum environment,” *Optik* **200**, 163429 (2020).
- [22] Y. Aharonov, D. Z. Albert, and L. Vaidman, “How the result of a measurement of a component of the spin of a spin-1/2 particle can turn out to be 100,” *Phys. Rev. Lett.* **60**, 1351 (1988).
- [23] R. Jozsa, “Complex weak values in quantum measurement,” *Phys. Rev. A* **76**, 044103 (2007).
- [24] Y. Wang, S. Chen, S. Wen, and H. Luo, “Realization of ultra-small stress birefringence detection with weak-value amplification technique,” *Appl. Phys. Lett.* **118**, 161104 (2021).
- [25] L. Zhang, A. Datta, and I. A. Walmsley, “Precision Metrology Using Weak Measurements,” *Phys. Rev. Lett.* **114**, 210801 (2015).
- [26] L. Li, Y. Li, Y. Zhang, S. Yu, C. Lu, N. Liu, J. Zhang, and J. Pan, “Phase amplification in optical interferometry with weak measurement,” *Phys. Rev. A* **97**, 033851 (2018).
- [27] J. S. Lundeen, B. Sutherland, A. Patel, C. Stewart, and C. Bamber, “Direct measurement of the quantum wavefunction,” *Nature* **474**, 188 (2011).
- [28] A. N. Jordan, J. Martínez-Rincón, and J. C. Howell, “Technical Advantages for Weak-Value Amplification: When Less Is More,” *Phys. Rev. X* **4**, 011031 (2014).
- [29] C. Ferrie and J. Combes, “Weak Value Amplification is Sub-optimal for Estimation and Detection,” *Phys. Rev. Lett.* **112**, 040406 (2014).
- [30] N. W. M. Ritchie, J. G. Story, and R. G. Hulet, “Realization of a measurement of a ‘weak value’,” *Phys. Rev. Lett.* **66**, 1107 (1991).
- [31] X. Qiu, L. Xie, X. Liu, L. Luo, Z. Li, Z. Zhang, and J. Du, “Precision phase estimation based on weak-value amplification,” *Appl. Phys. Lett.* **110**, 071105 (2017).
- [32] L. Xu, Z. Liu, A. Datta, G. C. Knee, J. S. Lundeen, Y. Lu, and L. Zhang, “Approaching Quantum-Limited Metrology with Imperfect Detectors by Using Weak-Value Amplification,” *Phys. Rev. Lett.* **125**, 080501 (2020).
- [33] L. Luo, L. Xie, J. Qiu, X. Zhou, X. Liu, Z. Li, Y. He, Z. Zhang, and H. Sun, “Simultaneously precise estimations of phase and amplitude variations based on weak-value amplification,” *Appl. Phys. Lett.* **114**, 111104 (2019).
- [34] P. Yin, W. Zhang, L. Xu, Z. Liu, W. Zhuang, L. Chen, M. Gong, Y. Ma, X. Peng, G. Li, J. Xu, Z. Zhou, L. Zhang, G. Chen, C. Li, and G. Guo, “Improving the precision of optical metrology by detecting fewer photons with biased weak measurement,” *Light Sci. Appl.* **10**, 819 (2021).
- [35] P. Yin, X. Zhao, Y. Yang, Y. Guo, W. Zhang, G. Li, Y. Han, B. Liu, J. Xu, G. Chiribella, G. Chen, C. Li, and G. Guo, “Experimental super-Heisenberg quantum metrology with indefinite gate order,” *Nat. Phys.* **19**, 1269 (2023).
- [36] N. Brunner and C. Simon, “Measuring Small Longitudinal Phase Shifts: Weak Measurements or Standard Interferometry?,” *Phys. Rev. Lett.* **105**, 010405 (2010).
- [37] X. Xu, Y. Kedem, K. Sun, L. Vaidman, C. Li, and G. Guo, “Phase Estimation with Weak Measurement Using a White Light Source,” *Phys. Rev. Lett.* **111**, 033604 (2013).
- [38] J. Huang, Y. Li, C. Fang, H. Li, and G. Zeng, “Toward ultra-high sensitivity in weak-value amplification,” *Phys. Rev. A* **100**, 012109 (2019).
- [39] G. Strübi and C. Bruder, “Measuring Ultrasmall Time Delays of Light by Joint Weak Measurements,” *Phys. Rev. Lett.* **110**, 083605 (2013).
- [40] H. Li, J. Huang, Y. Yu, Y. Li, C. Fang, and G. Zeng, “High-precision temperature measurement based on weak measurement using nematic liquid crystals,” *Appl. Phys. Lett.* **112**, 231901 (2018).
- [41] Y. Wang, J. Zhu, J. Wu, R. Ge, F. Gao, and Z. Zhang, “High-precision weak measurement sensing with adaptability in sensitivity,” *Appl. Phys. Lett.* **124**, 131102 (2024).
- [42] Y. Xu, L. Shi, T. Guan, C. Guo, D. Li, Y. Yang, X. Wang, L. Xie, Y. He, and W. Xie, “Optimization of a quantum weak measurement system with its working areas,” *Opt. Express* **26**, 21119 (2018).